Strength evolution of simulated carbonate-bearing faults: the role of normal stress and slip velocity.

Marco Mercuri[a*], Marco Maria Scuderi[a], Telemaco Tesei[b,1], Eugenio Carminati[a], Cristiano Collettini[a,b]

Affiliation addresses:

[a] Dipartimento di Scienze della Terra, Sapienza Università di Roma, Piazzale Aldo Moro 5, 00185, Rome, Italy

[b] Istituto Nazionale di Geofisica e Vulcanologia, Via di Vigna Murata 605, 00143, Rome, Italy

[1] Present address: Rock Mechanics Laboratory, Earth Sciences Department, Durham University, South Road, Durham, DH1 3LE, UK

E-mail addresses: marco.mercuri@uniroma1.it (M. Mercuri), marco.scuderi@uniroma1.it (M. M. Scuderi), telemaco.tesei@durham.ac.uk (T. Tesei), eugenio.carminati@uniroma1.it (E. Carminati), cristiano.collettini@uniroma1.it (C. Collettini)

*corresponding author: tel. +393342844933; e-mail: marco.mercuri@uniroma1.it; postal address: Piazzale Aldo Moro 5, Rome, Italy

keywords: calcite; microstructures; carbonate-bearing faults; friction

Abstract

A great number of earthquakes occur within thick carbonate sequences in the shallow crust. At the same time, carbonate fault rocks exhumed from a depth < 6 km (i.e., from seismogenic depths) exhibit the coexistence of structures related to brittle (i.e. cataclasis) and ductile deformation processes (i.e. pressure-solution and granular plasticity). We performed friction experiments on water-saturated simulated carbonate-bearing faults for a wide range of normal stresses (from 5 to 120 MPa) and slip velocities (from 0.3 to 100 μm/s). At high normal stresses (σ_n > 20 MPa) fault gouges undergo strain-weakening, that is more pronounced at slow slip velocities, and causes a significant reduction of frictional strength, from $\mu = 0.7$ to $\mu = 0.47$. Microstructural analysis show that fault gouge weakening is driven by deformation accommodated by cataclasis and pressure-insensitive deformation processes (pressure solution and granular plasticity) that become more efficient at slow slip velocity. The reduction in frictional strength caused by strain weakening behaviour promoted by the activation of pressure-insensitive deformation might play a significant role in carbonate-bearing faults mechanics.

1. Introduction

The characterization of the mechanical behaviour of carbonate-bearing faults is crucial to better understand the physical processes at the origin of earthquakes that nucleate or propagate through thick carbonate sequences. Notable examples are provided by the Aigion event in 1995 in Greece (Bernard et al., 1997), the Wenchuan earthquake in 2008 in China (Burchfiel et al., 2008) and by several events occurring in Italy such us: the Umbria-Marche in 1997-98 (Miller et al., 2004; Mirabella et al., 2008), the L'Aquila 2009 (e.g., Valoroso et al., 2014), the Emilia 2012 (Ventura and Di Giovanbattista 2013; Govoni et al., 2014) and the 2016-17 seismic sequence in the Amatrice and Norcia areas (Pizzi et al., 2017).

Deformation structures hosted in the outcrops of carbonate faults exhumed from < 6 km, i.e. from crustal depths where most of the seismic sequences in Italy nucleate or propagate, provide the opportunity to get insights into fault rocks and deformation mechanisms. Cataclastic processes that induce grain size reduction and slip localization along millimetric-to-micron thick principal shear

zones are widespread (e.g., Storti et al., 2003; Agosta and Aydin, 2006; De Paola et al., 2008; Smith et al., 2011; Collettini et al., 2014a). Cataclastic processes are often intimately associated with fluid assisted dissolution-precipitation and low temperature plasticity (Koopman, 1983; Kennedy and Logan, 1998; Tesei et al., 2013; Bullock et al., 2014; Wells et al., 2014; Viti et al., 2014). Diagnostic structures of fluid assisted dissolution-precipitation typically consist in pressure-solution seams (Fig. 1A) forming anastomosing foliations and slip surfaces (Fig. 1B). On the other hand, the evidences of granular plasticity are represented by twinning and sub-grains development (Fig. 1C; e.g., Kennedy and Logan, 1998; Siman-Tov et al., 2013; Collettini et al., 2014a). These observations, indicate that during fault activity different deformation mechanisms coexist and potentially control the resulting frictional strength at depth. These mechanisms can be grouped into pressure-sensitive, i.e., cataclasis, and pressure-insensitive, i.e., pressure solution flow and intracrystalline plasticity (Rutter, 1986).

Several experimental studies have investigated the effects of microscale deformation processes on the mechanics of carbonate bearing fault zone. At sub-seismic slip velocities and room temperature (i.e., $v < 1$ mm/s and $T \sim 25$ C^o), it has been shown that deformation is mainly accommodated by cataclasis through the localization of grain size reduction within the typical R-Y-B zones, in some cases associated with P-foliation (e.g. Logan et al., 1979, 1992). In addition, some studies have reported evidences for fluid-assisted dissolution and precipitation mechanisms (e.g. Carpenter et al., 2016), and granular plasticity represented by the formation of dense aggregates of nanograins (Tesei et al., 2017; Sagy et al., 2017). From these laboratory observations emerge the coexistence of pressure sensitive and insensitive processes governing the deformation style of carbonate-bearing simulated faults. This fault zone structure is commonly associated with high values of steady-state friction (μ_{ss}), that usually range between $\mu_{ss} \sim 0.7$ (dry conditions) to $\mu_{ss} \sim 0.6$ (saturated conditions) (Verberne et al., 2010, 2014; Carpenter et al., 2016). However, it has been shown that carbonate-bearing fault gouges can undergo significant frictional weakening under specific boundary conditions where pressure-insensitive deformation mechanisms are expected to be active, i.e., either high temperatures or slow deformation rates. For example, Verberne et al. (2015)

showed a decrease in the coefficient of friction with increasing temperature from $\mu_{ss} \sim 0.55$ at room temperature to $\mu_{ss} \sim 0.4$ at 200 ºC. Similarly, Carpenter et al. (2016) showed that the coefficient of friction at high normal stresses (i.e., $\sigma_n = 100$ MPa) decreases from $\mu_{ss} \sim 0.65$ at 1 mm/s down to $\mu_{ss} \sim 0.51$ at 0.1 μm/s. From these studies emerge that the activation of pressure insensitive micromechanical processes can decrease the frictional strength of carbonate-bearing fault zone with important implication for earthquake nucleation. However, these observations are sporadic and usually carried out from multiple stage experiments where the slip velocity is systematically varied to interrogate the velocity dependence of friction and/or frictional re-strengthening (e.g., Verberne et al., 2015; Carpenter et al., 2016). Each variation of slip velocity during the experiments can create a competition between micromechanical processes at the grain scale. In this context, the final microstructure is the sum of many processes that take place at different stages, making difficult to link the overall mechanical behaviour with the deformation mechanisms that accommodate shear.

In this work, we aim to better characterize the evolution of frictional strength along carbonate-bearing faults by performing shear experiments for a variety of normal stresses and slip velocities on simulated fault gouges of Carrara Marble. We inform the mechanical data with detailed microstructural analysis to shed light on the physico-chemical processes acting within carbonate-bearing fault zones varying the boundary conditions.

2. Methods

We performed rock deformation experiments on powdered Carrara Marble (> 98% $CaCO_3$ content) to simulate a carbonate-bearing fault gouge and to investigate its frictional properties. Experiments were conducted using a biaxial apparatus, BRAVA (Brittle Rock deformAtion Versatile Apparatus; Collettini et al., 2014b), in the double-direct shear configuration (Fig. 2). In this configuration two servo-controlled rams apply a horizontal and vertical load to the sample (Fig. 2A). Load was measured with ± 0.03 kN accuracy load cells mounted at the extremity of both pistons and in contact with the sample assembly (Fig. 2A). Linear Variable Displacement Transformers (Fig. 2A) measured horizontal and vertical displacements with a precision of ± 0.1 μm. Both horizontal and

100 vertical displacements were corrected taking in account for the elastic stiffness of the loading frame.
101 For horizontal loads, smaller than 50 kN, on the grounds of calibration tests (e.g., Collettini et al.,
102 2014b), elastic stiffness was 125.363 MPa/mm, while at higher loads we considered a stiffness value
103 of 416.558 MPa/mm due to the non-linear elastic deformation of the apparatus at small loads. For the
104 vertical piston, elastic stiffness was 116.801 MPa/mm for loads smaller than 50 kN, and 301.461
105 MPa/mm for higher loads. During experiments, we recorded loads and displacements, both in the
106 horizontal and vertical direction, with a sampling rate ranging from 1 to 100 Hz depending on the
107 target slip velocity (we registered at least one measurement every micron of slip).

108 Carrara Marble was preliminary grinded and passed through a 125 μm sieve. All the particles
109 that passed through the sieve were included in the starting material. Two identical, ~ 5 mm thick
110 gouge layers were constructed upon stainless steel forcing blocks with nominal frictional contact area
111 of 5 cm × 5 cm and both were assembled with the central forcing block composing a symmetric
112 assembly (Fig. 2B). To avoid slip at the interface between fault gouge and steel, and ensure that shear
113 localizes within the gouge, the surfaces of the forcing blocks were machined with grooves 0.8 mm
114 high and spaced 1 mm. To prevent excessive gouge extrusion during shear, a rubber membrane and
115 steel plates were fixed below and laterally of the sample assembly respectively (Fig. 2B).

116 We conducted 24 experiments (Table 1) at room temperature (i.e., ~25ºC) and water saturated
117 boundary conditions. As pore fluid, we used a $CaCO_3$-equilibrated water solution to simulate a
118 realistic pore fluid chemistry along shallow-crustal carbonate fault zones. For each experiment, once
119 the assembly was positioned within BRAVA, it was left saturating within a flexible membrane
120 containing $CaCO_3$ equilibrated water for 45 minutes under a normal load of 1 kN (Fig. 2B). At this
121 stage, we increased the normal stress to the desired target value that ranged between 5 and 120 MPa,
122 and left the sample to compact until a steady layer thickness was attained. The time for the compaction
123 of the sample was ~15 minutes, depending on the target normal stress. The vertical ram was then
124 advanced at constant displacement rate to apply shear stress and induce deformation within the
125 sample. We conducted experiments for a range of shear velocities between 0.3 μm/s and 100 μm/s

126 and a total shear displacement between 5 and 20 mm (Table 1). In addition, we performed unloading-
127 loading cycles every 5 mm of displacement (Fig. 3) to characterize stiffness and shear modulus of the
128 fault gouge but these data are not presented here.

129 At the end of each experiment, the deformed gouge layers were collected, impregnated with
130 epoxy resin and standard thin section were cut parallel to the slip direction for microstructural analysis
131 (optical microscope and Scanning Electron Microscope, SEM-backscattered electron mode). In
132 addition, gouge layers deformed in experiment b675 (see Table 1) were left drying and observed at
133 the SEM operated in secondary electron mode without the epoxy resin impregnation.

134 Normal stress (σ_n) was calculated dividing the applied normal load by the surface of the side
135 block (0.0025 m^2). Similarly, shear stress (τ) was calculated dividing vertical load by 0.005 m^2 (two
136 surfaces of application). We calculated the coefficient of friction dividing shear stress by normal
137 stress, and assuming no-cohesion for a powdered material. The values of the steady state friction
138 coefficients, μ_{ss} reported in the following, were measured as the average friction after the initial
139 loading phase (shear strain > 3), without considering the unloading-loading cycles (Fig. 3). For
140 experiments with a significant weakening after a shear strain of 3, this further evolution of friction
141 with strain is included as standard deviation from the mean value (e.g., vertical bars in Fig 4). Layer
142 thickness was calculated subtracting horizontal displacement values to the initial pre-shear value
143 measured using a calliper. In addition, we corrected layer thickness for geometrical thinning and
144 evaluated the shear strain accordingly (Scott et al., 1994).

145 **3. Results**

146 *3.1. Frictional behaviour*

147 The mechanical behaviour of simulated calcite fault gouges is controlled by applied normal
148 stress and imposed slip velocity. At low normal stress, e.g., σ_n = 10 MPa, the shear strength reaches
149 a steady state value (τ_{ss}) after a few millimetres of slip and it remains nearly constant until the end of
150 the experiment (Fig. 3A). This trend is independent on the applied slip velocity (Fig. 3A) and defines
151 a steady state coefficient of friction (μ_{ss}) of about 0.65 (Figs. 3A and 4B). Differently from the

experiments at low normal stress, at high normal stress, e.g., σ_n = 100 MPa, we document that shear strength evolves following three main stages. In stage one, after the initial nearly-elastic loading phase, the shear strength reaches a peak value (τ_{peak} in Fig. 3B) that corresponds to a friction of ~ 0.6 that is independent of the applied slip velocity (Fig. 3B). With increasing displacement, during stage two, we document a strain-weakening phase that depends on the imposed slip velocity. We observe that at slow slip velocities the strain weakening phase is more pronounced when compared with higher slip velocities (Fig. 3B). During stage three, fault gouge reaches a new steady state frictional sliding regime. As a consequence of stage two, the new values of frictional strength at steady state are lower for slower sliding velocities (Figs. 3B and 4B). For instance, at a slip velocity of 0.3 μm/s the corresponding steady state value of friction is ~ 0.5, which is lower when compared to that at a slip velocity of 10 μm/s where μ_{ss} ~ 0.6 (Figs. 3B and 4B).

The relationship between shear and normal stresses, when analysed in a Coulomb diagram, highlights two different regions (Fig. 4A). Below σ_n ~ 20 MPa, shear strength increases linearly with normal stress and is independent of the imposed slip velocity (Fig. 4A). The Coulomb failure envelope is described by a straight line with a slope μ = 0.64 (solid black line in Fig. 4A), representing the average coefficient of friction. Within this range of normal stresses, the coefficient of friction is independent on slip velocity and is comprised between 0.62 (σ_n = 5 MPa, v = 1 μm/s) and 0.66 (σ_n = 10 MPa, v = 10 μm/s) (Fig. 4B). For normal stress higher than 20 MPa, the relationship between shear strength and normal stress deviates from the linearity, in particular at slow slip velocity (Fig. 4A). Under the same imposed normal stress, slower slip velocities promote lower values of friction (Fig. 4B) and this is more pronounced at higher normal stresses (Fig. 4B). For example, at σ_n = 50 MPa, μ_{ss} decreases by ~11% (from 0.63 to 0.56) for slip velocity decreasing from 100 μm/s to 0.3 μm/s, whilst at σ_n = 100 MPa μ_{ss} decreases by ~19% (from 0.61 to 0.49) for the same range of slip velocities. For a fixed slip velocity, the steady-state friction decreases with increasing normal stress. This trend is more pronounced at slower slip velocities (Fig. 4B). For example, at slip velocity of 10 μm/s, friction decreases by ~ 5% (from 0.62 to 0.59) for normal stress increasing from 50 to 100

MPa, whilst at 0.3 μm/s, friction decreases by ~11% (from 0.56 to 0.49) for the same range of normal stresses (Fig 4B).

3.2. Microstructural observations

3.2.1. Low normal stress microstructures

At low normal stresses ($\sigma_n \leq 20$ MPa), deformation is localized in B and R_1 shear zones (Logan, 1979) that are observed at both high, v = 10 μm/s (Fig. 5A), and slow, v = 0.3 μm/s, slip velocity (Fig. 5C). B and R_1 consist of 100 to 200 μm-thick shear zones characterized by higher grain comminution when compared to the bulk gouge layer (Fig. 5B-D). In detail, these zones are characterized by angular grains typically smaller than 10 μm (Fig. 5B-D), whilst in the surrounding the grain size is larger and characterized by angular clasts with heterogeneous grain size distribution (Fig. 5A-C) resembling the undeformed gouge. Comparing gouge layers sheared at the same normal stress conditions but with different slip velocities, we do not observe substantial differences (Fig. 5).

3.2.2. High normal stress microstructures

The microstructures retrieved from experiments performed under high normal stresses ($\sigma_n >$ 20 MPa) show dramatically different features when compared with low normal stresses experiments. In general, we observe: 1) that shear deformation is distributed within the entire gouge, 2) the development of a pervasive anastomosing foliation and, 3) the development of very sharp principal slip zones with B geometry (Logan, 1979; Fig. 6A-B-C-D), associated with R_1 and Y fabric (Fig. 6A-B-C; see also Fig. 7C). The pervasive foliation is oriented at high angles to the ideal normal stress component of the shear couple (e.g. Ramsay, 1967) for both fast (Fig. 6A-B-E) and slow (Fig. 6C-D-F) slip velocities, showing a characteristic S-shape (Berthé et al., 1979; see Fig. 6) Apart from the common features mentioned above, only for the experiments at 10 μm/s, we observe pervasive grain comminution throughout the entire sample, although a few relict grains with dimensions of hundreds of microns are still present (Fig. 6A-B). At slow slip velocity (0.3 μm/s) larger grains are contained within a finer matrix and grain size reduction tends to increase approaching the B shear surface (Fig. 6C-D).

Looking at the details of fault zone structure we document the following features. (1) Large portions of the experimental faults are cemented (Fig. 7A). The cemented regions contain grain aggregates that are reworked by cataclastic processes (Fig. 7A) and are particularly evident in the sample collected at slow slip velocity (i.e., 0.3 μm/s). (2) The foliated zones consist of grains with sutured boundaries and local indentations (Fig. 7B). (3) The presence of grains that are folded along the pre-existing twinning planes (Fig 7C). Finally, when the principal slip zone is observed in plain view, it reveals (4) the presence of smooth striations (Fig. 7D) and packages characterized by very densely-packed nanoparticles with a polygonal geometry (10-150 nm in diameter; Fig. 7E).

4. Discussion

Our results show that the mechanical behaviour of simulated carbonate-bearing faults strongly depends on the applied normal stress and is modulated by the imposed slip velocity (Figs. 3-4). A marked change of behaviour occurs at a normal stress of ~ 20 MPa (Fig. 4) in agreement with previous experiments carried out on intact (Paterson, 1958; Fredrich et al., 1989) and powdered (Carpenter et al., 2016) Carrara Marble. In particular, at relatively low values of normal stress ($\sigma_n \leq 20$ MPa) we observe a nearly constant steady-state shear strength that is not affected by accumulated shear displacement and imposed slip velocity (Fig. 3A). This behaviour favours a linear relationship between shear stress and normal stress described by a failure envelope with a slope of $\mu = 0.64$ (Fig. 4A), which is in general agreement with other studies on calcite-rich lithologies (e.g., Verberne et al., 2010, 2014; Carpenter et al., 2014; Tesei et al., 2014; Chen et al., 2015). Furthermore, we observe that deformation localizes within shear bands characterized by strong grain size reduction and with B and R_1 geometries (Fig. 5). The coupling of the mechanical behaviour and microstructural observations indicates that, at low normal stress, the mechanical behaviour is controlled by pressure-sensitive deformation (i.e., cataclasis) with localization along B and R shear planes.

For the experiments performed at higher normal stress (i.e., $\sigma_n > 20$ MPa), we observe that shear strength evolves in three stages with accumulated displacement, reaching a peak that is followed by a strain-weakening phase before attaining a steady state value (Fig. 3B). As a result of this

230 behaviour, we document a non-linear relationship between shear and normal stress that is more
231 pronounced at slow slip velocities (Fig. 4A). The observed weakening can be interpreted by
232 considering the interplay of different processes: 1) cataclasis, 2) fluid-rock interaction, which favours
233 fluid assisted dissolution and precipitation processes, and 3) intragranular plasticity. Coupling
234 mechanical data with microstructural observations we note that shear is accommodated by a
235 distributed deformation, accomplished through pervasive grain size reduction and the development
236 of a pervasive foliation (Fig. 6). The anastomosing foliation (Fig. 6), the presence of densely-packed
237 grains with sutured contacts and local grain indentations (Fig. 7B) suggest that fluid assisted
238 dissolution and precipitation processes played an important role, inducing compaction and dissolution
239 of smaller grains (e.g., Rutter 1983; Gratier and Gamond 1990). Large cemented portions of the
240 experimental fault (Fig. 7A) represent a direct evidence of calcite precipitation and strengthens the
241 hypothesis of the activity of fluid-assisted diffusion mass transfer (i.e., pressure-solution + transport
242 + precipitation; Rutter 1983; Gratier et al., 2013). A further evidence of the role played by fluid
243 assisted diffusion mass transfer in fault weakening can be inferred comparing mechanical data
244 retrieved from an experiment conducted under nominally dry conditions (i.e., relative humidity <5%)
245 and at high normal stress with the saturated experiments (Fig. 8). Under dry conditions the shear
246 strength is high, $\mu = 0.7$, and we do not observe the characteristic strain weakening reported under
247 saturated conditions (Fig. 8). Furthermore, the presence of folded grains (Fig. 7C) and densely-packed
248 nanoparticles (Fig. 7E) that form the principal slip surfaces (Fig. 7D) indicates that granular plasticity
249 was also active during deformation (Kennedy and Logan, 1998; Tesei et al., 2017).
250
251 To summarize, our microstructural observations suggest that at high normal stress (i.e., $\sigma_n >$
252 20 MPa) pressure-insensitive deformation mechanisms (i.e., pressure-solution flow and intra-
253 crystalline plasticity; Rutter, 1986) work together with pressure-sensitive mechanisms (i.e.,
254 cataclasis) in accommodating shear deformation. We suggest that with increasing normal stress, the
255 activation of pressure-insensitive deformation mechanisms is responsible for the strain weakening

256 phase (Fig. 3B) and for the transition from a linear relationship between shear strength and normal
257 stress (i.e., purely pressure-sensitive) to a more non-linear relationship (i.e., less pressure-sensitive).
258 Since both the strain weakening phase and the departure from the linear behaviour are more evident
259 at slow slip velocities (Figs. 3B and 8), we posit that time-dependent mechanisms (i.e., pressure-
260 solution flow and granular plasticity) increase their role in accommodating shear deformation with
261 decreasing slip velocity because of the longer contact time between grains that favours their
262 dissolution.

263 The range of normal stresses investigated in our experiments together with saturated fluid
264 conditions allow us to get insights on the mechanics of carbonate-bearing faults at seismogenic depths
265 (between 1 and ~ 10 km). Our results suggest that the activation of fluid assisted diffusion mass
266 transfer and grain plasticity can significantly reduce the frictional strength of carbonate-bearing
267 faults, from 0.7 to 0.47 in friction, facilitating fault slip. This observation has important implications
268 for our understanding of frictional processes associated with the nucleation of unstable slip, when
269 slip velocity is still slow. In this context, fluid rock interaction weakens the fault favouring the onset
270 of slip. Then, as slip accelerates, the onset of dynamic slip will be controlled by the rate dependence
271 of friction and the local generation of high pore fluid pressure, which can promote seismic slip even
272 if the fault is characterized by rate strengthening behaviour (Scuderi et al., 2017). This mechanism is
273 appealing in relation to the seismicity observed along the Apennines, where the coupling of high fluid
274 pressure (e.g., Miller et al., 2004; Lucente et al., 2010) and fluid-rock interaction, can potentially
275 promote earthquake.

276 **5. Conclusion**

277 We investigated the coupling between mechanical and microstructural features of carbonate-
278 bearing faults by performing shear experiments on powdered Carrara Marble under saturated
279 boundary conditions. We explored a range of normal stresses (5 MPa $\leq \sigma_n \leq$ 120 MPa) and slip
280 velocities (0.3 μm/s $\leq$ v $\leq$ 100 μm/s) to shed light on the time-dependent physico-chemical processes
281 that control the evolution of fault zone strength. We observe that an increase in normal stress promote

fault zone weakening through the activation of pressure-insensitive deformation mechanisms. Comparing microstructures from low to high normal stress we report a transition from localized to distributed deformation associated with the development of an anastomosed foliation. We suggest that the different micromechanical processes, such as pressure solution flow and granular plasticity, accommodating shear deformation are responsible for the evolution from a linear to a non-linear Coulomb envelope.

Since the coexistence of cataclastic and pressure-insensitive deformation is a typical feature of carbonate fault rocks exhumed from seismogenic depths, we suggest that the shear strength weakening documented in our experiments is relevant for the mechanics of faults hosted in carbonate sequences.

Acknowledgments

We thank Dr. Steven Smith and an anonymous reviewer, whose comments greatly improved the manuscript. We also thank Brett Carpenter and Carolina Giorgetti for useful discussion, Domenico Mannetta (Mimmo) for high quality thin sections preparation, and Manuela Nazzari for her technical assistance with the SEM at the HP-HT laboratory at INGV, Rome. This research was supported by ERC Starting Grant nr. 259256 “GLASS” and Sapienza Progetti Ricerca Ateneo 2015 to CC, Horizon 2020 under the Marie Sklodowska-Curie action, No. 748400 STRAIN to TT, and Horizon 2020 under the Marie Sklodowska-Curie action, No. 656676 FEAT to MMS.

References

Agosta, F., Aydin, A., 2006. Architecture and deformation mechanism of a basin-bounding normal fault in Mesozoic platform carbonates, central Italy. Journal of Structural Geology 28, 1445–1467. doi:10.1016/j.jsg.2006.04.006

Bernard, P., Briole, P., Meyer, B., Lyon-Caen, H., Gomez, J.M., Tiberi, C., Berge, C., Cattin, R., Hatzfeld, D., Lachet, C., Lebrun, B., Deschamps, A., Courboulex, F., Larroque, C., Rigo, A., Massonnet, D., Papadimitriou, P., Kassaras, J., Diagourtas, D., Makropoulos, K., Veis, G., Papazisi, E., Mitsakaki, C., Karakostas, V., Papadimitriou, E., Papanastassiou, D., Chouliaras, M.,

308 Stavrakakis, G., 1997. The Ms=6.2, June 15, 1995 Aigion earthquake (Greece): evidence for low
309 angle normal faulting in the Corinth rift. Journal of Seismology 1, 131–150.
310 Berthé, Choukroune, Jegouzo, 1979. Orthogneiss, mylonite and non coaxial deformation of granites:
311 the example of the South Armorican Shear Zone. Journal of Structural Geology 1, 31–42.
312 https://doi.org/10.1016/0191-8141(79)90019-1
313 Bullock, R.J., De Paola, N., Holdsworth, R.E., Trabucho-Alexandre, J., 2014. Lithological controls
314 on the deformation mechanisms operating within carbonate-hosted faults during the seismic cycle.
315 Journal of Structural Geology 58, 22–42. doi:10.1016/j.jsg.2013.10.008
316 Burchfiel, B.C., Royden, L.H., van der Hilst, R.D., Hager, B.H., Chen, Z., King, R.W., Li, C., Lü, J.,
317 Yao, H., Kirby, E., 2008. A geological and geophysical context for the Wenchuan earthquake of
318 12 May 2008, Sichuan, People's Republic of China. GSA Today 18, 4. doi:10.1130/gsatg18a.1
319 Carpenter, B.M., Collettini, C., Viti, C., Cavallo, A., 2016. The influence of normal stress and sliding
320 velocity on the frictional behaviour of calcite at room temperature: insights from laboratory
321 experiments and microstructural observations. Geophysical Journal International 205, 548–561.
322 doi:10.1093/gji/ggw038
323 Carpenter, B.M., Scuderi, M.M., Collettini, C., Marone, C., 2014. Frictional heterogeneities on
324 carbonate-bearing normal faults: Insights from the Monte Maggio Fault, Italy. Journal of
325 Geophysical Research: Solid Earth 119, 9062–9076. doi:10.1002/2014jb011337
326 Chen, J., Verberne, B.A., Spiers, C.J., 2015. Interseismic re-strengthening and stabilization of
327 carbonate faults by “non-Dieterich” healing under hydrothermal conditions. Earth and Planetary
328 Science Letters 423, 1–12. doi:10.1016/j.epsl.2015.03.044
329 Collettini, C., Carpenter, B.M., Viti, C., Cruciani, F., Mollo, S., Tesei, T., Trippetta, F., Valoroso, L.,
330 Chiaraluce, L., 2014a. Fault structure and slip localization in carbonate-bearing normal faults: An
331 example from the Northern Apennines of Italy. Journal of Structural Geology 67, 154–166.
332 doi:10.1016/j.jsg.2014.07.017

Collettini, C., Di Stefano, G., Carpenter, B., Scarlato, P., Tesei, T., Mollo, S., Trippetta, F., Marone, C., Romeo, G., Chiaraluce, L., 2014b. A novel and versatile apparatus for brittle rock deformation. International Journal of Rock Mechanics and Mining Sciences 66, 114–123. doi:10.1016/j.ijrmms.2013.12.005

De Paola, N., Collettini, C., Faulkner, D.R., Trippetta, F., 2008. Fault zone architecture and deformation processes within evaporitic rocks in the upper crust. Tectonics 27. doi:10.1029/2007tc002230

De Paola, N., Holdsworth, R.E., Viti, C., Collettini, C., Bullock, R., 2015. Can grain size sensitive flow lubricate faults during the initial stages of earthquake propagation? Earth and Planetary Science Letters 431, 48–58. doi:10.1016/j.epsl.2015.09.002

Fredrich, J.T., Evans, B., Wong, T.-F., 1989. Micromechanics of the brittle to plastic transition in Carrara marble. Journal of Geophysical Research 94, 4129–4145.

Govoni, A., Marchetti, A., De Gori, P., Di Bona, M., Lucente, F.P., Improta, L., Chiarabba, C., Nardi, A., Margheriti, L., Agostinetti, N.P., Di Giovambattista, R., Latorre, D., Anselmi, M., Ciaccio, M.G., Moretti, M., Castellano, C., Piccinini, D., 2014. The 2012 Emilia seismic sequence (Northern Italy): Imaging the thrust fault system by accurate aftershock location. Tectonophysics 622, 44–55. doi:10.1016/j.tecto.2014.02.013

Gratier, JP, Gamond, JF, 1990. Transition between seismic and aseismic deformation in the upper crust. Geological Society, London, Special Publications 54, 461–473. https://doi.org/10.1144/gsl.sp.1990.054.01.42

Gratier, J. P., Dysthe, D.K., Renard, F., 2013. The Role of Pressure Solution Creep in the Ductility of the Earth's Upper Crust, Advances in Geophysics, Advances in Geophysics. Elsevier.

Kennedy, L., Logan, J., 1998. Microstructures of cataclasites in a limestone-on-shale thrust fault: implications for low-temperature recrystallization of calcite. Tectonophysics 295, 167–186. https://doi.org/10.1016/S0040-1951(98)00119-X

Koopman, A, 1983. Detachment tectonics in the central Apennines, Italy. https://doi.org/10.1145/1056635.1056636

Logan, J.M., Dengo, C.A., Higgs, N.G., Wang, Z.Z., 1992. Fabrics of Experimental Fault Zones: Their Development and Relationship to Mechanical Behavior, International Geophysics 51, 33-67

Logan, J.M., Friedman, M., Higgs, C., Dengo, C., Shimamoto, T., 1979. Experimental studies of simulated gouge and their application to studies of natural fault zones, in: Proc. 8th Conf. on Analysis of Actual Fault Zones in Bedrock, pp. 305–343.

Miller, S.A., Collettini, C., Chiaraluce, L., Cocco, M., Barchi, M.R., Kaus, B.J.P., 2004. Aftershocks driven by a high-pressure CO2 source at depth. Nature 427, 724–727. doi:10.1038/nature02251

Mirabella, F., Barchi, M.R., Lupattelli, A., Stucchi, E., Ciaccio, M.G., 2008. Insights on the seismogenic layer thickness from the upper crust structure of the Umbria-Marche Apennines (central Italy). Tectonics 27. doi:10.1029/2007tc002134

Paterson, M.S., 1958. Experimental deformation and faulting in Wombeyan Marble. Geological Society of America Bulletin 69, 465-476.

Pizzi, A., Di Domenica, A., Gallovič, F., Luzi, L., Puglia, R., 2017. Fault Segmentation as Constraint to the Occurrence of the Main Shocks of the 2016 Central Italy Seismic Sequence. Tectonics 84, 6140. doi:10.1002/2017tc004652

Ramsay, J., 1967. Folding and fracturing of rocks.

Rutter, E.H., 1986. On the nomenclature of mode of failure transitions in rocks. Tectonophysics 122, 381–387.

Rutter, E.H., 1983. Pressure solution in nature, theory and experiment. Journal of the Geological Society 140, 725–740.

Sagy, A., Tesei, T., Collettini, C., 2017. Fault-surface geometry controlled by faulting mechanisms: Experimental observations in limestone faults. Geology 45, 851–854. https://doi.org/10.1130/g39076.1

384 Scott, D.R., Marone, C.J., Sammis, C.G., 1994. The apparent friction of granular fault gouge in
385 sheared layers. Journal of Geophysical Research 99, 7231. doi:10.1029/93jb03361
386 Scuderi, M.M., Collettini, C., Marone, C., 2017. Frictional stability and earthquake triggering during
387 fluid pressure stimulation of an experimental fault. Earth and Planetary Science Letters 477, 84–
388 96. https://doi.org/10.1016/j.epsl.2017.08.009
389 Sibson, R.H., 1977. Fault rocks and fault mechanisms. Journal of the Geological Society 133, 191–
390 213. doi:10.1144/gsjgs.133.3.0191
391 Siman-Tov, S., Aharonov, E., Sagy, A., Emmanuel, S., 2013. Nanograins form carbonate fault
392 mirrors. Geology 41, 703–706. doi:10.1130/g34087.1
393 Smith, S.A.F., Billi, A., Di Toro, G., Spiess, R., 2011. Principal Slip Zones in Limestone:
394 Microstructural Characterization and Implications for the Seismic Cycle (Tre Monti Fault, Central
395 Apennines, Italy). Pure and Applied Geophysics 168, 2365–2393. doi:10.1007/s00024-011-0267-
396 5
397 Storti, F., Billi, A., Salvini, F., 2003. Particle size distributions in natural carbonate fault rocks:
398 insights for non-self-similar cataclasis. Earth and Planetary Science Letters 206, 173–186.
399 doi:10.1016/s0012-821x(02)01077-4
400 Tesei, T., Carpenter, B.M., Giorgetti, C., Scuderi, M.M., Sagy, A., Scarlato, P., Collettini, C., 2017.
401 Friction and scale-dependent deformation processes of large experimental carbonate faults.
402 Journal of Structural Geology 100, 12–23. doi:10.1016/j.jsg.2017.05.008
403 Tesei, T., Collettini, C., Barchi, M.R., Carpenter, B.M., Di Stefano, G., 2014. Heterogeneous strength
404 and fault zone complexity of carbonate-bearing thrusts with possible implications for seismicity.
405 Earth and Planetary Science Letters 408, 307–318. doi:10.1016/j.epsl.2014.10.021
406 Tesei, T., Collettini, C., Viti, C., Barchi, M.R., 2013. Fault architecture and deformation mechanisms
407 in exhumed analogues of seismogenic carbonate-bearing thrusts. Journal of Structural Geology
408 55, 167–181. doi:10.1016/j.jsg.2013.07.007

409 Valoroso, L., Chiaraluce, L., Collettini, C., 2014. Earthquakes and fault zone structure. Geology 42,
410 343–346. doi:10.1130/g35071.1
411 Ventura, G., Di Giovambattista, R., 2012. Fluid pressure, stress field and propagation style of
412 coalescing thrusts from the analysis of the 20 May 2012 ML5.9 Emilia earthquake (Northern
413 Apennines, Italy). Terra Nova 25, 72–78. doi:10.1111/ter.12007
414 Verberne, B.A., de Bresser, J.H.P., Niemeijer, A.R., Spiers, C.J., de Winter, D.A.M., Plümper, O.,
415 2013. Nanocrystalline slip zones in calcite fault gouge show intense crystallographic preferred
416 orientation: Crystal plasticity at sub-seismic slip rates at 18–150 °C. Geology 41, 863–866.
417 doi:10.1130/g34279.1
418 Verberne, B.A., He, C., Spiers, C.J., 2010. Frictional Properties of Sedimentary Rocks and Natural
419 Fault Gouge from the Longmen Shan Fault Zone, Sichuan, China. Bulletin of the Seismological
420 Society of America 100, 2767–2790. doi:10.1785/0120090287
421 Verberne, B.A., Niemeijer, A.R., de Bresser, J.H.P., Spiers, C.J., 2015. Mechanical behavior and
422 microstructure of simulated calcite fault gouge sheared at 20-600°C: Implications for natural faults
423 in limestones. J. Geophys. Res. 120, 8169–8196. doi:10.1002/2015jb012292
424 Verberne, B.A., Spiers, C.J., Niemeijer, A.R., De Bresser, J.H.P., De Winter, D.A.M., Plümper, O.,
425 2014. Frictional Properties and Microstructure of Calcite-Rich Fault Gouges Sheared at Sub-
426 Seismic Sliding Velocities. Pure and Applied Geophysics 171, 2617–2640. doi:10.1007/s00024-
427 013-0760-0
428 Viti, C., Collettini, C., Tesei, T., 2014. Pressure solution seams in carbonatic fault rocks: mineralogy,
429 micro/nanostructures and deformation mechanism Contributions to Mineralogy and Petrology
430 167. doi:10.1007/s00410-014-0970-1
431 Wells, R.K., Newman, J., Wojtal, S., 2014. Microstructures and rheology of a calcite-shale thrust
432 fault. Journal of Structural Geology 65, 69 – 81. https://doi.org/10.1016/j.jsg.2014.04.002
433

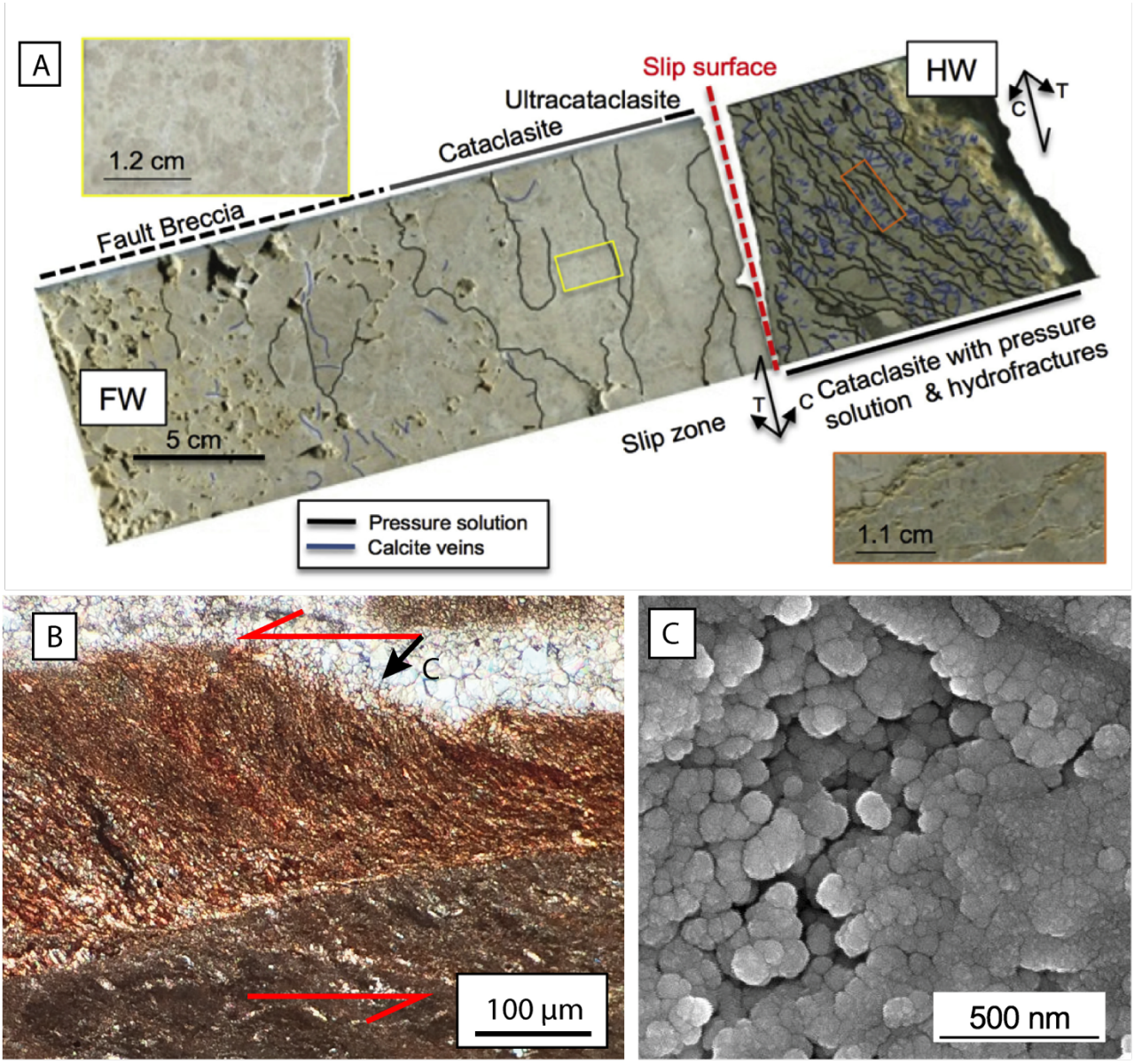

Figure 1 – Coexistence of pressure-sensitive (i.e., cataclasis) and pressure-insensitive deformation in carbonate fault rocks exhumed from seismogenic depths in the Northern Apennines. A) Typical cataclastic products (Fault Breccia, Cataclasite and Ultracataclasite; Sibson, 1977) are found together with pressure-solution seams in a transect through the core Monte Maggio fault, which display strong localization of slip also at the sample scale (Collettini et al., 2014a). B) Anastomosed foliation with S-geometry nearly orthogonal to the compression component (C) of the shear couple. This microstructure formed by pressure-solution and re-precipitation processes along a carbonate/clay fault (Tesei et al., 2013; Viti et al., 2014). C) Nanometer-scale subgrains in the Monte Maggio fault (De Paola et al., 2015).

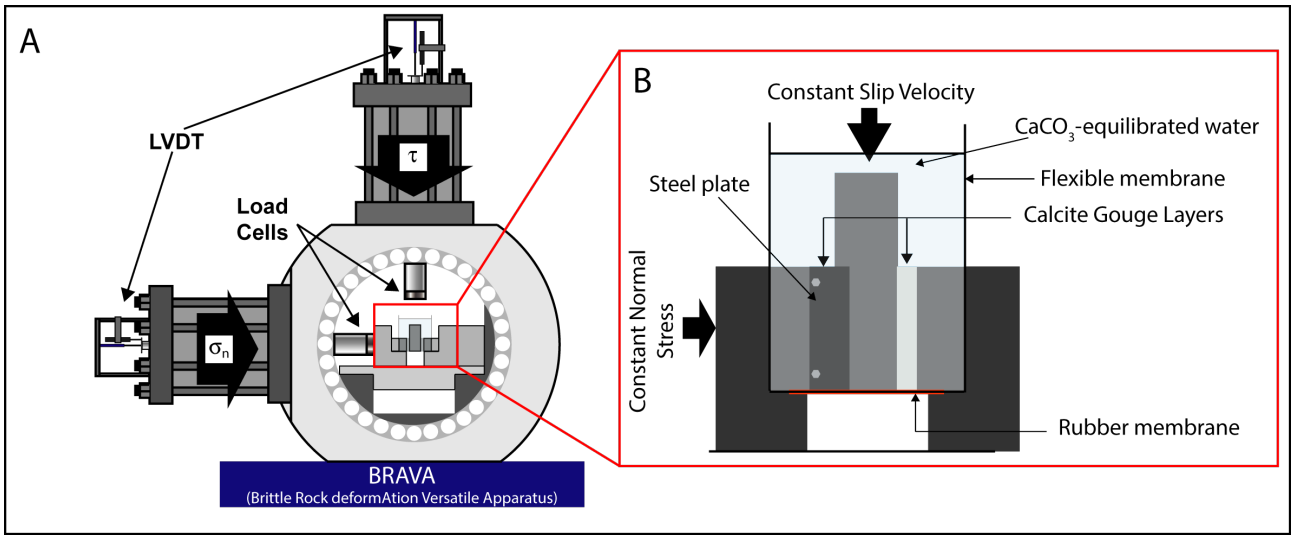

444

445 Fig. 2 – (A) The biaxial servo-controlled apparatus used for this study (BRAVA in INGV, Rome;
446 Collettini et al., 2014b). Horizontal and vertical load cells and LVDTs control and measure
447 respectively loads and displacements. (B) The double direct shear configuration: two identical layers
448 of gouge are comprised between three steel forcing blocks; a constant horizontal load is applied
449 laterally and the central block is moved downward with constant velocity inducing symmetric shear
450 within gouge layers.

451

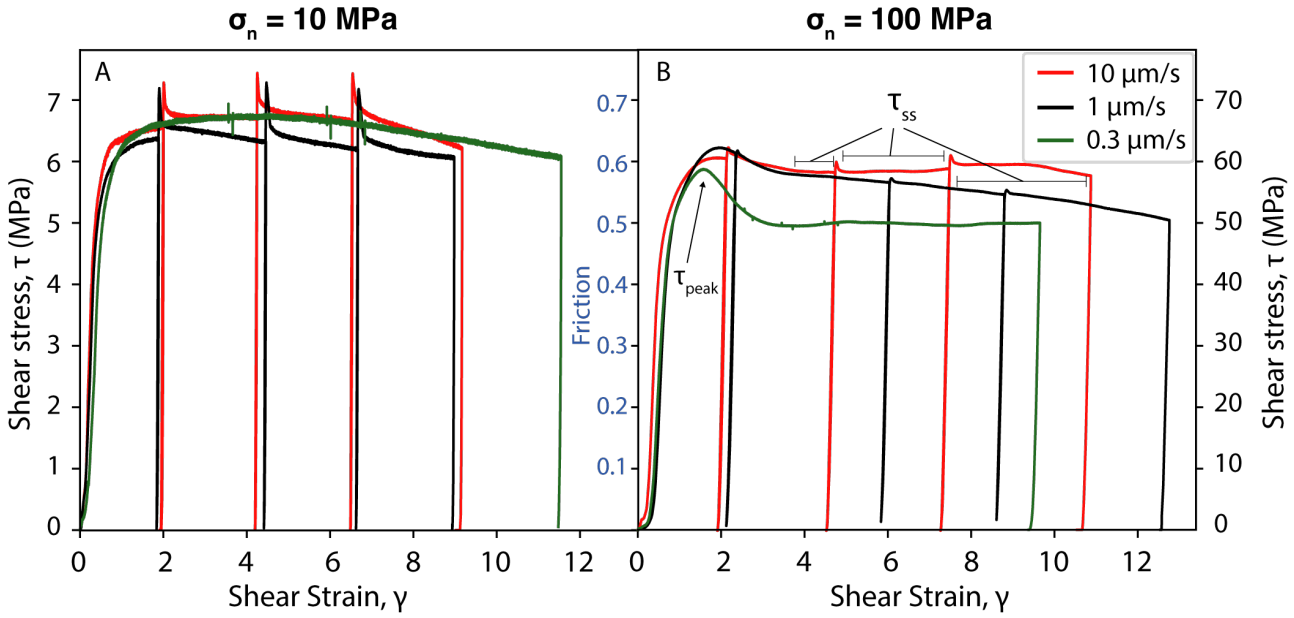

452

453 Fig. 3 – Shear stress (τ) and friction (μ) evolution with shear strain (γ) for experiments performed at

454 (A) 10 and (B) 100 MPa at different slip velocities. The portion of the curve where peak and steady-

455 state shear stress were collected, see methods for details, is marked by τ_{peak} and τ_{ss} respectively.

456

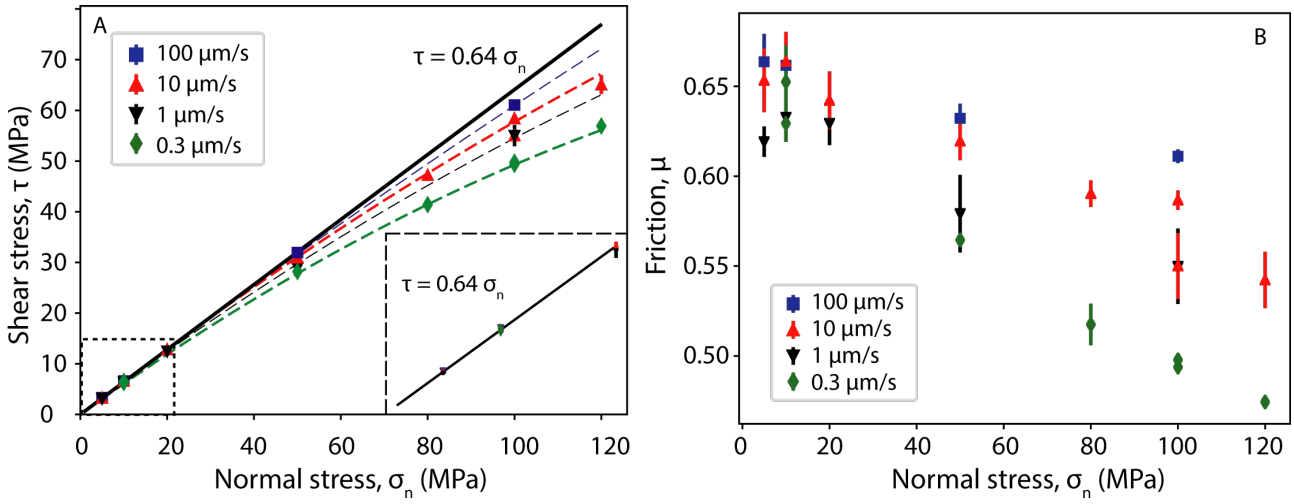

457

458 Fig. 4 – A) Evolution of shear strength τ vs. normal stress σ_n, for different slip velocities. Black line
459 represents Mohr-Coulomb failure envelope for experiments performed at $\sigma_n \leq 20$ MPa (inset). At
460 high normal stresses and slow slip velocities, a second-order polynomial function provides a better
461 fit than the classical linear Coulomb regression data. B) Mean steady-state friction coefficient, μ_{ss},
462 plotted against normal stress for different slip velocities. The variability of friction observed during
463 each experiment is represented by the vertical bars (see methods for details).

464

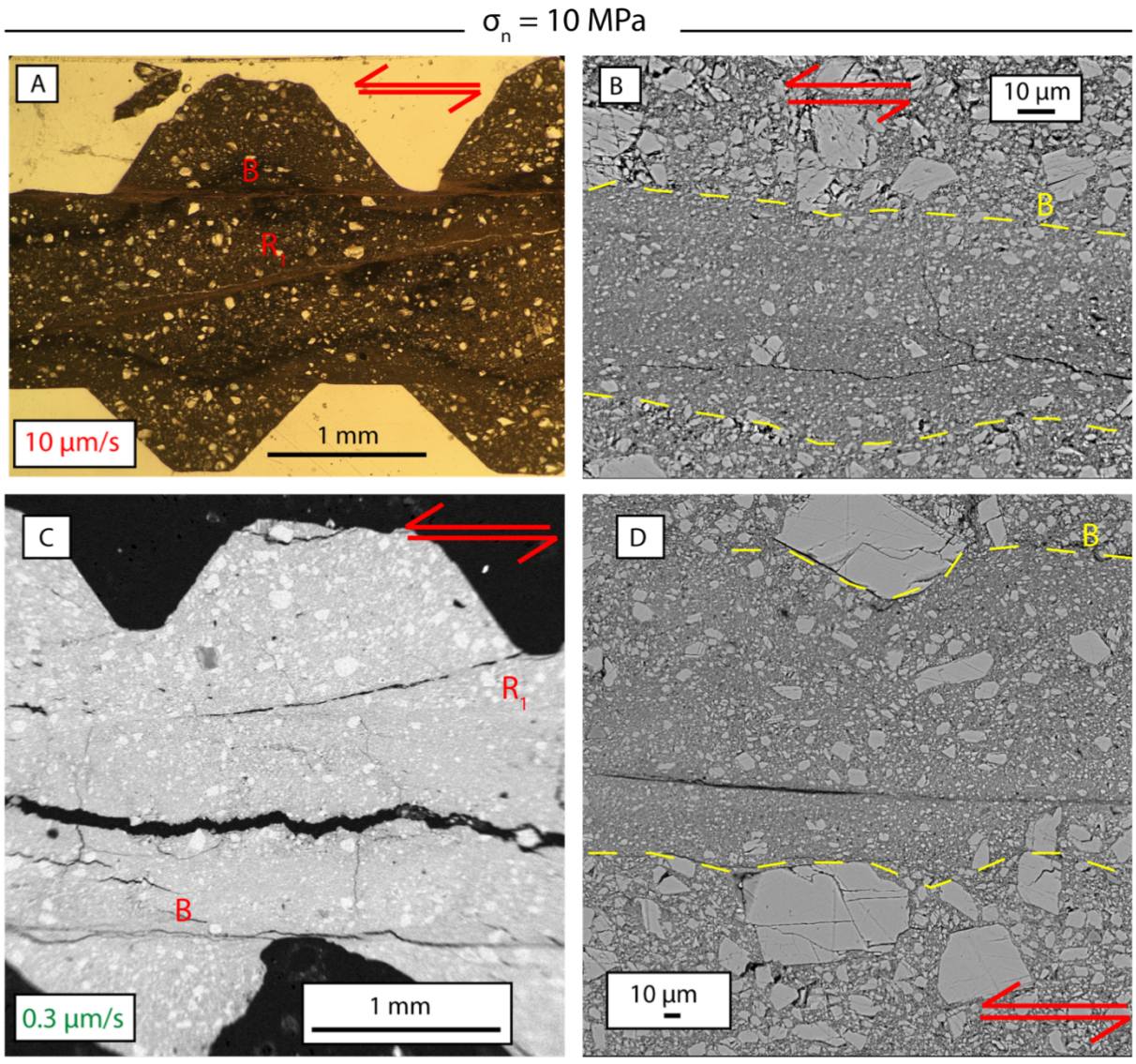

Fig. 5 – Microstructures of simulated calcite fault gouges deformed at low normal stress (σ_n = 10 MPa) and at slip velocity of 10 µm/s (A, B) and 0.3 µm/s (C, D). Figures A and B are from experiment b555, whilst figures C and D are from the experiment b651 (see Table 1). Deformation localizes into B and R_1 zones (A, C) that are represented by 100 to 200 µm-thick shear zones characterized by higher grain comminution than the bulk gouge layer (B, D). Figure A is an optical micrograph (plane polarized light), whilst B, C, D are from SEM microscope in backscattered mode.

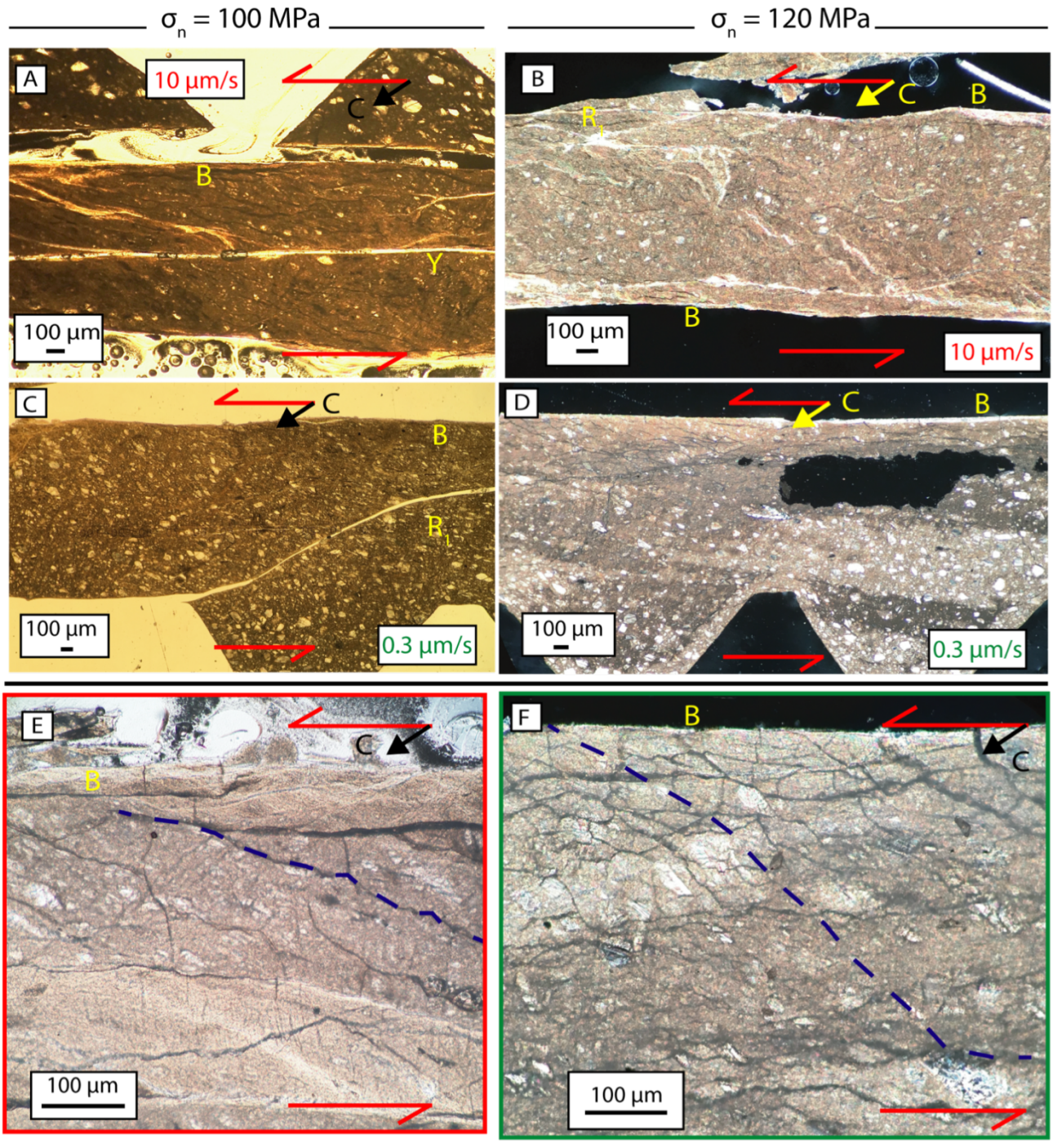

Fig. 6 – Optical micrographs of simulated fault gouges deformed at a relatively high normal stress (σ_n = 100 MPa for the left column and σ_n = 120 MPa on the right one) and at slip velocity of 10 µm/s (A, B, E) and 0.3 µm/s (C, D, F). Figures A, C and E derive from observations at plane polarized light, whilst figures B, D and E are from observation at cross polarized light. The micrographs are derived from experiments b564 (A, E), b641 (B), b639 (C) and b640 (D, F); experiments are listed in Table 1. Deformation is distributed within the entire gouge layer (A, B, C. D) and is characterized by

480 strong grain size reduction and the development of an anastomosed foliation, which is interpreted as
481 oriented orthogonal to the normal stress component, C, of the shear couple. Grain comminution is
482 more pronounced at higher slip velocities (Fig. A vs C and Fig. B vs. D). A detail of the anastomosed
483 foliation at a slip velocity of 10 μm/s and 0.3 μm/s is presented in Fig. E and F respectively.
484

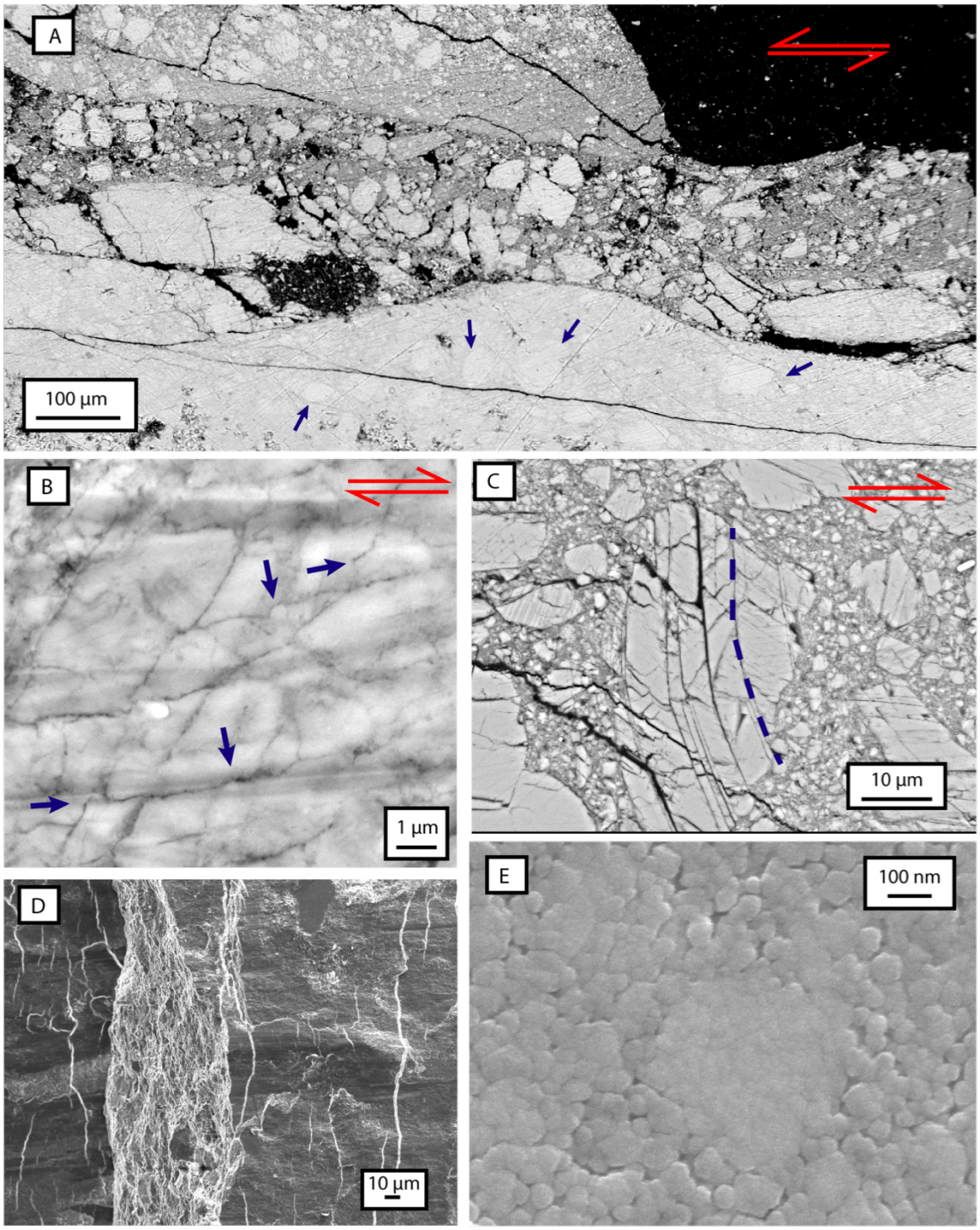

Fig. 7 – SEM micrographs in simulated calcite fault gouges deformed under relatively high normal stresses, i.e., 120 (A, B) and 100 MPa (C, D, E). A) Large cemented portion of the gouge deformed during the experiment b640 (Table 1). Blue arrows indicate grains within the cemented portion. B) Sutured grain contacts with indentations (blue arrows) in the experiment b640 (Table 1). C) Folded calcite grain in the experiment b564 (Table 1). Shear zones are often striated (D) and constituted by dense aggregates of nanograins (E); the figures D and E are from the experiment b675.

492

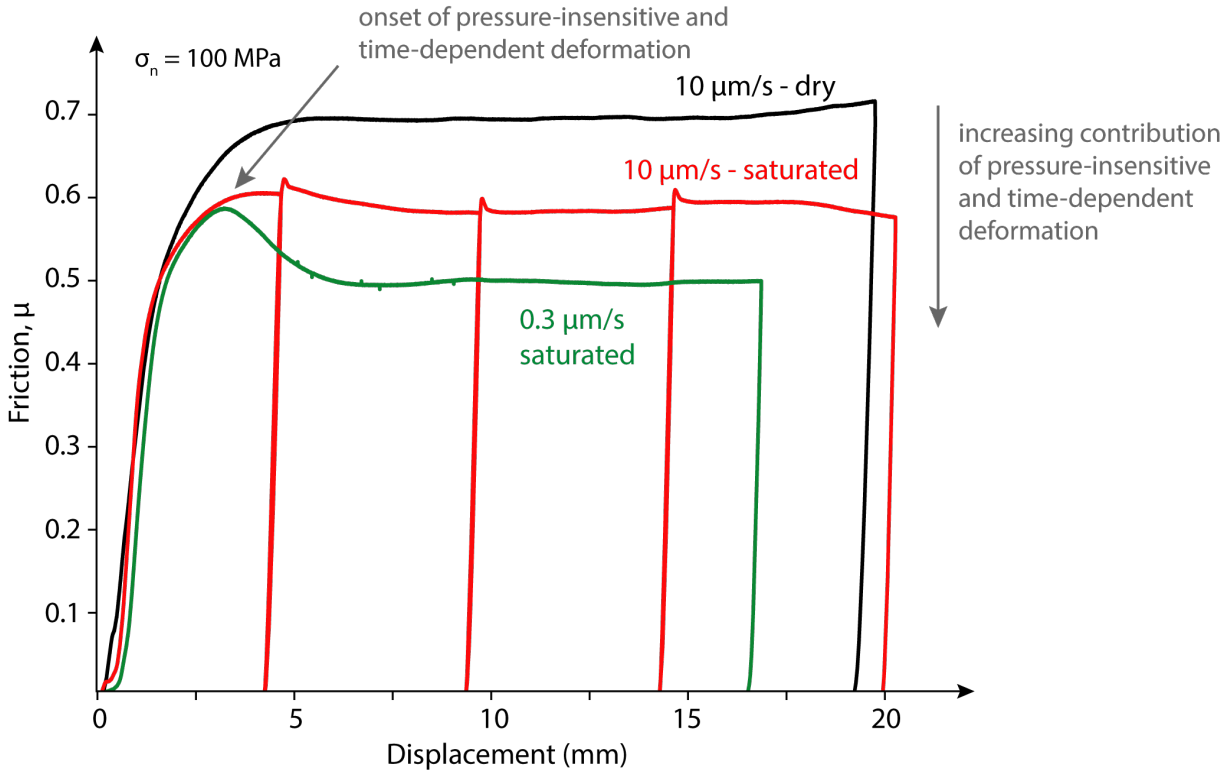

493

494 Fig. 8 – Evolution of friction with displacement for experiments at normal stress of 100 MPa in
495 saturated conditions at a slip velocity of 0.3 µm/s (green) and 10 µm/s (red) and for an experiment
496 performed dry and at slip velocity of 10 µm/s.

497

Experiment name	Normal stress, (σ_n) (MPa)	Slip velocity (μm/s)	Total Displacement (mm)	Total shear strain (γ)
b555	10	10	19.6	10.3
b556	20	10	19.9	8.5
b561	50	10	19.9	10.4
b562	5	10	20.3	5.8
b563	10	100	20.3	9.9
b564	100	10	20.3	12.3
b566	50	100	20.2	10.4
b567	5	100	20.2	7.9
b568	100	100	19.8	11.6
b600	100	1	21.3	14.6
b602	50	1	20.4	9.1
b603	10	1	21.2	10.1
b604	10	0.3	8.2	3.6
b605	50	0.3	7.2	3.8
b606	100	0.3	5.7	3.9
b631	20	1	19.2	8.5
b638	5	1	19.6	10.3
b639	100	0.3	16.9	9.6
b640	120	0.3	13.8	7.6
b641	120	10	18.5	12.0
b642	80	10	18.6	13.0
b643	80	0.3	18.4	11.9

b651	10	0.3	20.0	11.6
b675	100	10	13.6	9.7

498 Table 1 – Summary of experiments and boundary conditions. All tests were conducted under $CaCO_3$-

499 equilibrated water saturated conditions.